V International Conference on Computational Methods for Coupled Problems in Science and Engineering
COUPLED PROBLEMS 2013
S. Idelsohn, M. Papadrakakis and B. Schrefler (Eds)

A BODNER-PARTOM VISCO-PLASTIC DYNAMIC SPHERE BENCHMARK PROBLEM

Brandon M. Chabaud*, Jerry S. Brock† and Todd O. Williams†

*Los Alamos National Laboratory (LANL)
Los Alamos, NM 87545, United States
email: chabaud@lanl.gov

†Los Alamos National Laboratory (LANL)
Los Alamos, NM 87545, United States
email: jsbrock@lanl.gov, oakhill@lanl.gov

Key words: spherical shell, analytic solution, Bodner-Partom model

Abstract. Developing benchmark analytic solutions for problems in solid and fluid mechanics is very important for the purpose of testing and verifying computational physics codes. Our primary objective in this research is to obtain a benchmark analytic solution to the equation of motion in radially symmetric spherical coordinates. An analytic solution for the dynamic response of a sphere composed of an isotropic visco-plastic material and subjected to spherically symmetric boundary conditions is developed and implemented. The radial displacement u is computed by solving the equation of motion, a linear second-order hyperbolic PDE. The plastic strains ε^p_{rr} and $\varepsilon^p_{\theta\theta}$ are computed by solving two non-linear first-order ODEs in time. We obtain a solution for u in terms of the plastic strain components and boundary conditions in the form of an infinite series. Computationally, at each time step, we set up an iteration scheme to solve the PDE-ODE system. The linear momentum equation is solved using the plastic strains from the previous iteration, then the plastic strain equations are solved numerically using the new displacement. We demonstrate the accuracy and convergence of our benchmark solution under spatial mesh, time step, and eigenmode refinement.

1 INTRODUCTION

In this paper we derive an analytic solution for the geometrically linear dynamic response of a sphere for the purpose of comparing it to the results from computational physics codes. An example of a spherical solid mechanics problem is the Blake problem, which has been of considerable long-term [1, 2] and recent [3] interest to the scientific community. The Blake problem consists of a spherical inclusion within an infinite medium.

In contrast, the dynamic sphere problem considered here develops an analytic solution for the dynamic response of a spherically symmetric shell composed of a visco-plastic, isotropic material and subjected to prescribed time-dependent boundary conditions imposed at both the inner and outer radii (r_i and r_o, respectively). The boundary conditions are arbitrary and may be any one of the following: applied radial stresses, applied radial strains, or applied radial displacements. The physical problem under consideration is illustrated in the figure below.

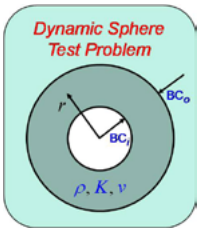

Figure 1: 2-D schematic of dynamic sphere problem.

In spherical coordinates the stress-strain constitutive relation for a visco-plastic isotropic material is given by the linear system [4]

$$\begin{aligned} \sigma &= C\varepsilon^e && (1)\\ &= C(\varepsilon - \varepsilon^p) && (2)\\ &= C\varepsilon - C\varepsilon^p && (3)\\ &= C\varepsilon + \lambda^p, && (4)\\ \lambda^p &= -C\varepsilon^p. && (5) \end{aligned}$$

Here σ is the total stress tensor, λ^p is the plastic stress tensor, ε is the total linear strain tensor, ε^e is the elastic strain tensor, ε^p is the plastic strain tensor, and C is the constant fourth-order stiffness tensor. For a spherically symmetric shell, the shear components of the strain ($\varepsilon_{r\theta}$, $\varepsilon_{r\varphi}$, $\varepsilon_{\theta r}$, $\varepsilon_{\theta\varphi}$, $\varepsilon_{\varphi r}$, $\varepsilon_{\varphi\theta}$) are all identically zero, so the only stresses on the shell are normal stresses (σ_{rr}, $\sigma_{\theta\theta}$, $\sigma_{\varphi\varphi}$). Also, by the isotropic symmetry of the material, the tangential stresses and strains satisfy $\sigma_{\theta\theta} = \sigma_{\varphi\varphi}$, $\lambda^p_{\theta\theta} = \lambda^p_{\varphi\varphi}$, $\varepsilon_{\theta\theta} = \varepsilon_{\varphi\varphi}$, and $\varepsilon^p_{\theta\theta} = \varepsilon^p_{\varphi\varphi}$.

The governing equations of the dynamic sphere problem come from the balance laws of continuum mechanics. We formulate these laws in material coordinates, so the balance of mass equation is automatically satisfied. Additionally, we assume that the shell is kept at constant temperature, so the balance of energy equation can also be neglected. The initial-boundary value problem (IBVP) to be solved, which comes from the equation of motion, is

$$c_r^{-2}u_{tt} = u_{rr} + \frac{2}{r}u_r - \frac{2}{r^2}u + c_r^{-2}f_\lambda; \quad t > 0, r_i \le r \le r_o \tag{6}$$

$$f_\lambda = \frac{1}{\rho_0}\left[\frac{\partial \lambda^p_{rr}}{\partial r} + \frac{2}{r}(\lambda^p_{rr} - \lambda^p_{\theta\theta})\right]; \quad t > 0, r_i \le r \le r_o \tag{7}$$

$$u(r,0) = 0, \quad u_t(r,0) = 0; \quad r_i \leq r \leq r_o \tag{8}$$

$$\alpha_B u_r(r_B,t) + \beta_B u(r_B,t) = \mathrm{BC}_B(t) - d\lambda^p_{rr}(r_B,t); \quad B = i,o;\ t > 0 \tag{9}$$

In this system $u(r,t)$ is the radial displacement, and in (8) we have set initial displacement and velocity equal to zero. f_λ is the contribution of the plastic stress to the acceleration of the material. This term is given by (7), where f_λ is defined in terms of the radial plastic stress λ^p_{rr} and the tangential plastic stress $\lambda^p_{\theta\theta}$. From (5), we see that the plastic stresses are given in terms of the plastic strains by

$$\lambda^p_{rr} = -C_{rrrr}\varepsilon^p_{rr} - 2C_{rr\theta\theta}\varepsilon^p_{\theta\theta}, \quad \lambda^p_{\theta\theta} = -C_{rr\theta\theta}\varepsilon^p_{rr} - (C_{rrrr} + C_{rr\theta\theta})\varepsilon^p_{\theta\theta}. \tag{10}$$

Boundary conditions are given by (9), where $B = i$ refers to conditions imposed on the inner surface and $B = o$ refers to conditions imposed on the outer surface. $\mathrm{BC}_i(t)$ and $\mathrm{BC}_o(t)$ are prescribed time-dependent boundary conditions imposed on the inner and outer surfaces, respectively. The speed of sound through the material is $c_r = \sqrt{\frac{C_{rrrr}}{\rho_0}}$, and ρ_0 is the initial density. For later times, the density ρ is given by the linearized Lagrangian mass equation

$$\rho = \rho_0/(1 + \varepsilon_{rr} + 2\varepsilon_{\theta\theta}). \tag{11}$$

The values of the material constants α_i, α_o, β_i, and β_o depend on whether displacement (Dirichlet), strain (Neumann), or stress (Robin) boundary conditions are imposed [5, 6, 7]. The parameter d that appears in (9) is equal to zero when Dirichlet or Neumann conditions are imposed and is equal to unity when Robin conditions are imposed.

The system of equations given by (6)-(10) is not complete. Evolution equations must be given for the plastic strain components. In this work the plastic strain tensor evolves according to the Bodner-Partom (BP) model for visco-plasticity [8]. For a radially symmetric spherical shell problem, the equations are

$$\dot{\varepsilon}^p_{rr} = S_{rr}\gamma, \quad \dot{\varepsilon}^p_{\theta\theta} = S_{\theta\theta}\gamma; \tag{12}$$

$$\varepsilon^p_{rr}(r,0) = 0, \quad \varepsilon^p_{\theta\theta}(r,0) = 0; \tag{13}$$

$$S_{rr} = \sigma_{rr} - \frac{1}{3}(\sigma_{rr} + 2\sigma_{\theta\theta}), \quad S_{\theta\theta} = \sigma_{\theta\theta} - \frac{1}{3}(\sigma_{rr} + 2\sigma_{\theta\theta}); \tag{14}$$

In this system $\dot{\varepsilon}^p_{rr} = \frac{\partial \varepsilon^p_{rr}}{\partial t}$ and $\dot{\varepsilon}^p_{\theta\theta} = \frac{\partial \varepsilon^p_{\theta\theta}}{\partial t}$ are the plastic strain rates. (13) gives initial conditions for the ODEs (12). According to the BP model, these rates are proportional to the stress deviator components S_{rr} and $S_{\theta\theta}$, which are defined by (14). The factor γ that appears in (12) is the proportionality coefficient for the BP model. We refer the reader to [8] for the details of how to compute it.

2 ANALYTIC SOLUTION

Our primary objective is to obtain an analytic expression for $u(r,t)$ in terms of λ^p_{rr} and $\lambda^p_{\theta\theta}$ that solves the system (6)-(9). In order to obtain a solution, we introduce the variable

$w(r,t) = r^{1/2}u(r,t)$. The transformed equation of motion is

$$rc_r^{-2}w_{tt} = rw_{rr} + w_r - \frac{\mu^2}{r}w + r^{3/2}f, \tag{15}$$

where $\mu = 3/2$ and $f = c_r^{-2}f_\lambda$. We decompose w into two terms $w = \overline{w} + \tilde{w}$. We take $\overline{w}(r,t) = \gamma_0(t) + \gamma_1(t)r$ and choose the coefficients γ_0 and γ_1 so that $\overline{w}$ satisfies the transformed boundary condition equations. This amounts to solving the linear system

$$\begin{bmatrix} \beta_o^* & \alpha_o^* + \beta_o^* r_o \\ \beta_i^* & \alpha_i^* + \beta_i^* r_i \end{bmatrix} \begin{bmatrix} \gamma_0(t) \\ \gamma_1(t) \end{bmatrix} = \begin{bmatrix} k_i(t) \\ k_o(t) \end{bmatrix} \tag{16}$$

where

$$\alpha_i^* = \frac{\alpha_i}{\sqrt{r_i}},\ \alpha_o^* = \frac{\alpha_o}{\sqrt{r_o}},\ \beta_i^* = \frac{\beta_i}{\sqrt{r_i}} - \frac{\alpha_i}{2r_i^{3/2}},\ \beta_o^* = \frac{\beta_o}{\sqrt{r_o}} - \frac{\alpha_o}{2r_o^{3/2}} \tag{17}$$

are transformed boundary condition coefficients and

$$k_i(t) = \mathrm{BC}_i(t) - d\lambda_{rr}^p(r_i,t),\ k_o(t) = \mathrm{BC}_o(t) - d\lambda_{rr}^p(r_o,t) \tag{18}$$

are transformed boundary conditions. From this system and the form chosen for $\overline{w}$, it is easy to show that $\overline{w}$ can be expressed as

$$\overline{w}(r,t) = [\gamma_{0,o} + \gamma_{1,o}r]k_o(t) + [\gamma_{0,i} + \gamma_{1,i}r]k_i(t), \tag{19}$$

where $\gamma_{0,o}$, $\gamma_{1,o}$, $\gamma_{0,i}$, and $\gamma_{1,i}$ are constants. The transformed IVBP solution $\tilde{w}(r,t)$ satisfies

$$rc_r^{-2}\tilde{w}_{tt} = L(\tilde{w}) + \tilde{f}, \tag{20}$$

$$\tilde{w}(r,0) = w(r,0) - \overline{w}(r,0), \quad \tilde{w}_t(r,0) = w_t(r,0) - \overline{w}_t(r,0), \tag{21}$$

$$\alpha_B^*\tilde{w}_r(r_B,t) + \beta_B^*\tilde{w}(r_B,t) = 0, \quad B = i,o \tag{22}$$

where

$$L(w) = rw_{rr} + w_r - \frac{\mu^2}{r}w \tag{23}$$

is the Sturm-Liouville operator and

$$\tilde{f} = L(\overline{w}) - c_r^{-2}r\overline{w}_{tt} + r^{3/2}f. \tag{24}$$

Thus we have reduced the problem of finding the displacement u to the problem of solving the homogeneous IBVP (20)-(22). The solution to (20)-(22) has the form

$$\tilde{w}(r,t) = \sum_{n=1}^{\infty} a_n(t)\psi_n(r), \tag{25}$$

where $\psi_n(r)$ are eigenfunctions which are computed from solving the autonomous problem (with $\tilde{f} \equiv 0$) and $a_n(t)$ are time-dependent coefficients that satisfy the second-order-in-time ODE

$$\frac{d^2 a_n}{dt^2} + c_r^2 \lambda_n a_n = F_n. \tag{26}$$

Here λ_n is the eigenvalue corresponding to eigenfunction ψ_n and $F_n(t)$ is a source function given by

$$F_n(t) = c_r^2 \frac{\int_{r_i}^{r_o} \tilde{f}(r,t)\psi_n(r)dr}{\int_{r_i}^{r_o} r\psi_n^2(r)dr}. \tag{27}$$

The eigenfunctions are given by

$$\psi_n(r) = c_{1,n} J_\mu(r\sqrt{\lambda_n}) + c_{2,n} Y_\mu(r\sqrt{\lambda_n}), \tag{28}$$

where J_μ and Y_μ are Bessel functions of order μ of the first and second kind, respectively, and $c_{1,n}$ and $c_{2,n}$ are constants that depend on eigenvalue λ_n. The solution to the ODE (26) is given by

$$a_n(t) = c_{3,n} \cos c_r\sqrt{\lambda_n}t + c_{4,n} \sin c_r\sqrt{\lambda_n}t + \frac{1}{c_r\sqrt{\lambda_n}} \int_0^t F_n(\tau) \sin c_r\sqrt{\lambda_n}(t-\tau)d\tau, \tag{29}$$

where the constants $c_{3,n}$ and $c_{4,n}$ are given by

$$c_{3,n} = \frac{\int_{r_i}^{r_o} r\tilde{w}(r,0)\psi_n(r)dr}{\int_{r_i}^{r_o} r\psi_n^2(r)dr}, \quad c_{4,n} = \frac{1}{c_r\sqrt{\lambda_n}} \frac{\int_{r_i}^{r_o} r\tilde{w}_t(r,0)\psi_n(r)dr}{\int_{r_i}^{r_o} r\psi_n^2(r)dr}. \tag{30}$$

For the derivation of this solution, we refer the reader to [9, 10]. Thus we have an analytic expression for the displacement $u = r^{-1/2}(\overline{w} + \tilde{w})$ in terms of λ_{rr}^p and $\lambda_{\theta\theta}^p$ solving the original IBVP (6)-(9).

3 COMPUTATION OF ANALYTIC SOLUTION

Our ultimate objective in developing the analytic solution derived in the previous section is to compare it with results of computational physics codes. The analytic solution of the dynamic sphere problem is cast as an infinite series solution. In practice, however, we truncate the Fourier-Bessel series solution (25) after a finite number of terms. We also notice that our benchmark solution requires us to evaluate several space and time integrals, so computationally we must apply spatial and time meshes. Additionally, the plastic stress and strain equations (10)-(14) must be solved numerically. There is no analytic expression for these quantities.

In this section we describe the algorithm we use to compute all relevant quantities at each time step. For any integer $n \geq 1$, we assume that the solution has been computed up to time t_{n-1}. At each time step, we iterate between the equation of motion (6) and the plasticity equations (10)-(14) to obtain a solution. For convenience we define the plastic strain increment to be $\Delta\varepsilon^p(t_n) = \varepsilon^p(t_n) - \varepsilon^p(t_{n-1})$. The procedure is described in the following algorithm.

Algorithm 1 (Decoupling Equations at Time Step n) *Compute u, ε^p, and λ^p at time t_n.*
Set $\varepsilon_{rr}^{p,(0)}(t_n) = \varepsilon_{rr}^p(t_{n-1})$, $\varepsilon_{\theta\theta}^{p,(0)}(t_n) = \varepsilon_{\theta\theta}^p(t_{n-1})$, $\lambda_{rr}^{p,(0)}(t_n) = \lambda_{rr}^p(t_{n-1})$, $\lambda_{\theta\theta}^{p,(0)}(t_n) = \lambda_{\theta\theta}^p(t_{n-1})$.
for** iteration $k = 1, 2, \cdots$ **do
Compute $u^{(k)}(t_n)$ with analytic solution using $\lambda_{rr}^{p,(k-1)}(t_n)$, $\lambda_{\theta\theta}^{p,(k-1)}(t_n)$ in plastic force term.
Substitute $u^{(k)}$ and $\lambda^{p,(k-1)}$ into (12) and solve for $\varepsilon_{rr}^{p,(k)}(t_n)$, $\varepsilon_{\theta\theta}^{p,(k)}(t_n)$ using explicit forward Euler finite difference method.
Substitute $\varepsilon_{rr}^{p,(k)}(t_n)$, $\varepsilon_{\theta\theta}^{p,(k)}(t_n)$ into (10) to obtain $\lambda_{rr}^{p,(k)}(t_n)$, $\lambda_{\theta\theta}^{p,(k)}(t_n)$.
If $||\Delta\varepsilon^{p,(k)}(t_n) - \Delta\varepsilon^{p,(k-1)}(t_n)||_{L^\infty} \leq \text{tol}||\Delta\varepsilon^{p,(k-1)}(t_n)||_{L^\infty}$,
Set $u(t_n) = u^{(k)}(t_n)$, $\varepsilon^p(t_n) = \varepsilon^{p,(k)}(t_n)$, $\lambda^p(t_n) = \lambda^{p,(k)}(t_n)$.
Exit loop.
end for

In this algorithm, the L^∞ norms are computed over the spatial mesh and tol is a user-defined tolerance that determines when the iteration scheme converges.

We point out here that the analytic solution for u given in the previous section contains spatial integrals of spatial derivatives of λ_{rr}^p and temporal integrals of time derivatives of λ_{rr}^p. It is possible to use finite difference approximations to evaluate these derivatives. However, the best approach, leading to the fastest convergence, is to use integration by parts to remove as many plastic stress derivatives as possible from the analytic solution. We also note that when evaluating the plastic stress integrals, sixth-order Newton-Cotes or a similar high-order numerical quadrature scheme must be used to compute the integrals accurately. A lower-order quadrature scheme, such as the trapezoid rule, will result in nonphysical oscillations.

4 SELF-CONVERGENCE ANALYSIS

In this section we consider a test problem and examine how the computed solution converges with respect to space and time meshes as well as with respect to number of terms (eigenmodes) taken in the series solution. We impose stress boundary conditions on the inner and outer radii, so $d = 1$ in (9). We take the interior of the shell to be a void, so $\text{BC}_i(t) = 0$, and on the outer radius we take a time-varying smooth jump stress condition. Figure 2 gives a plot of the outer radius stress boundary condition. The curve takes the form of a hyperbolic tangent function. The exact form and parameters used for this boundary condition can be found in Section 2 of [11].

In all of our simulations, we take inner radius $r_i = 1$ cm, outer radius $r_o = 2$ cm, and we run our simulations out to a final time of $T = 3.5$ microseconds. The constants appearing in the boundary conditions (9) are given by

$$\alpha_i = \alpha_o = C_{rrrr}, \quad \beta_i = \frac{2}{r_i} C_{rr\theta\theta}, \quad \beta_o = \frac{2}{r_o} C_{rr\theta\theta}. \tag{31}$$

The stiffness tensor coefficients that appear in the problem are computed in terms of

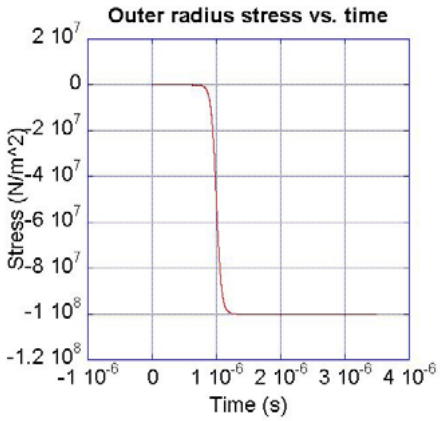

Figure 2: Stress boundary condition on outer radius.

engineering constants [12]. For an isotropic material, the coefficients are given by

$$C_{rrrr} = K + \frac{4}{3}G, \quad C_{rr\theta\theta} = K - \frac{2}{3}G, \tag{32}$$

where the constants K and G are the bulk and shear moduli of the material, respectively. Table 1 gives the parameter values, which are taken from Case (d) of [11], that we use in our simulations. The parameter values given in the table do not correspond to any real material. Our only interest here is verification of physics codes.

Table 1: Parameters used in convergence simulations.

Parameter	Value
r_i	1 cm
r_o	2 cm
ρ_0	1000 kg/m^3
K	100 GPa
G	60 GPa

In order to assess the convergence of our benchmark analytic solution, we will take both a qualitative and quantitative approach. Qualitatively, we will simply plot relevant physical quantities for different size meshes and show that the plots converge. To demonstrate quantitative convergence, we will compute L^∞ norms of percent errors with respect to extremely refined reference solutions and show that these norms are small. For example, the L^∞ norm of the percent error between the displacement u and a reference

displacement u_{ref} is computed by the expression

$$\% \text{ error} = \frac{||u - u_{ref}||_{L^\infty}}{||u_{ref}||_{L^\infty}} \times 100\%, \tag{33}$$

where we take the L^∞ norm either in time over the interval $(0, T)$ along shell boundaries or in space over the spherical shell (r_i, r_o). The quantities of interest in our convergence analysis are displacement, velocity, and radial and tangential total strain, plastic strain, and stress.

We begin by considering spatial convergence. To assess convergence qualitatively, we ran simulations with $nl = 500$ eigenmodes, $nt = 8000$ equally spaced time intervals, and uniform spatial meshes with varying numbers of intervals. The top two plots in Figure 3

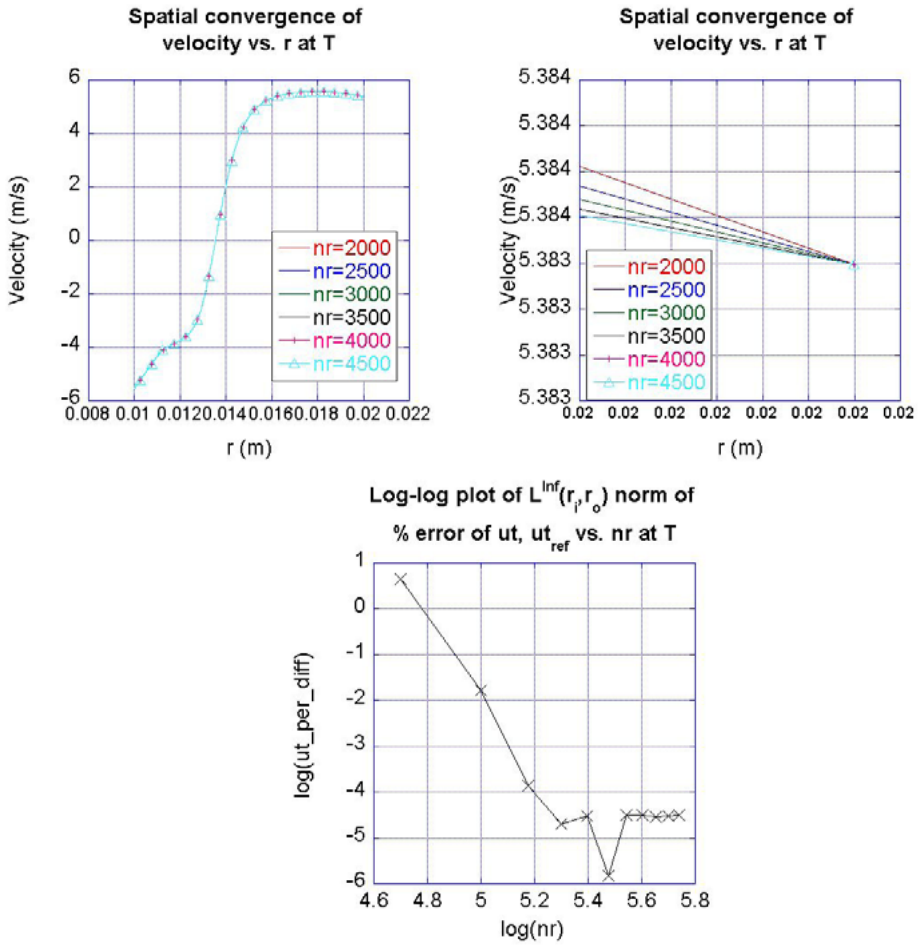

Figure 3: Top Left: Spatial convergence plot of u_t vs. r through radial shell at time $T = 3.5$ microseconds. Top Right: Zoomed-in plot of u_t. Bottom: Log-log plot of $L^\infty(r_i, r_o)$ percent error of u_t through shell vs. nr.

show the velocity u_t vs. radial position r through the shell at final computation time $T = 3.5$ microseconds for uniform spatial meshes of size $nr = 2000$, 2500, 3000, 3500, 4000, and 4500 intervals. The zoomed-in plot at the top right of the figure shows that the velocity profile is converging as the mesh is refined. The bottom plot in Figure 3 gives a log-log plot of the $L^\infty(r_i, r_o)$ norm of the percent error of u_t vs. nr for nr varying from 500 to 5500 in increments of 500. A mesh of $nr = 6000$ intervals was used to compute a reference solution for (33). We notice that the percent error corresponding to $nr = 3500$ is approximately $10^{-4.5}\%$. Of all the quantities of interest, the one with the highest error through the shell is radial plastic strain, with an $L^\infty(r_i, r_o)$ norm of percent error of approximately $10^{-3.5}\%$ for $nr = 3500$. Computing $L^\infty(0, T)$ norms of percent errors on the inner and outer radii gives even smaller errors. Therefore, because these errors are so small, we take $nr = 3500$ as an appropriate spatial resolution for a "converged" solution.

To assess temporal convergence, we ran simulations with $nr = 3500$ uniform spatial intervals, $nl = 500$ eigenmodes, and uniform time meshes of varying sizes. The top two plots in Figure 4 show the radial plastic strain ε^p_{rr} vs. time t at the inner radius r_i for time meshes of size $nt = 5500$, 6000, 6500, 7000, and 7500 uniform time steps. The zoomed-in plot at the top right of the figure shows that the radial plastic strain profile is converging as smaller step sizes are used. The bottom plot in Figure 4 gives a log-log plot of the $L^\infty(0, T)$ norm of the percent error of ε^p_{rr} at r_i vs. nt for nt varying from 2500 to 7500 in increments of 500. A mesh of $nt = 8000$ intervals was used to compute a reference solution for (33). We notice that the percent error corresponding to $nt = 6500$ is less than 0.01%. Radial plastic strain has the largest $L^\infty(0, T)$ norm of percent error at r_i of all the quantities of interest. We obtain similar results when we compute $L^\infty(0, T)$ norms of percent errors at the outer radius r_o. Computing $L^\infty(r_i, r_o)$ norms of percent errors at final time T, we find once again that ε^p_{rr} exhibits the largest error, this time with error approximately 0.1%. Because these errors are so small, we take $nt = 6500$ as an appropriate temporal resolution for a "converged" solution.

Finally, we assess eigenmode convergence. We ran simulations with $nr = 3500$ uniform spatial intervals, $nt = 6500$ uniform time steps, and varying numbers of eigenmodes. The top two plots in Figure 5 show the radial strain ε_{rr} vs. time t at the outer radius r_o for $nl = 100$, 150, 200, 250, and 300 eigenmodes. The zoomed-in plot at the top right of the figure shows that the radial strain profile is converging as more eigenmodes are used. The bottom plot in Figure 5 gives a log-log plot of the $L^\infty(0, T)$ norm of the percent error of ε_{rr} at r_o vs. nl for nl varying from 100 to 450 in increments of 50. A reference solution with $nl = 500$ eigenmodes was used to compute the percent error in (33). We notice that the percent errors for all of the eigenmodes shown in the log-log plot are less than $10^{-5}\%$. For $nl = 300$ (fourth mark from the right in the log-log plot), the error is less than $10^{-6.5}\%$. Of all the quantities of interest, velocity has the largest $L^\infty(0, T)$ norm of percent error at r_o, slightly less than $10^{-5}\%$ when $nl = 300$. In the $L^\infty(0, T)$ norm at r_i, velocity still has the largest error, approximately $10^{-3.6}\%$ when $nl = 300$. In the $L^\infty(r_i, r_o)$ norm at final time T, the quantity with the largest error is radial stress, with

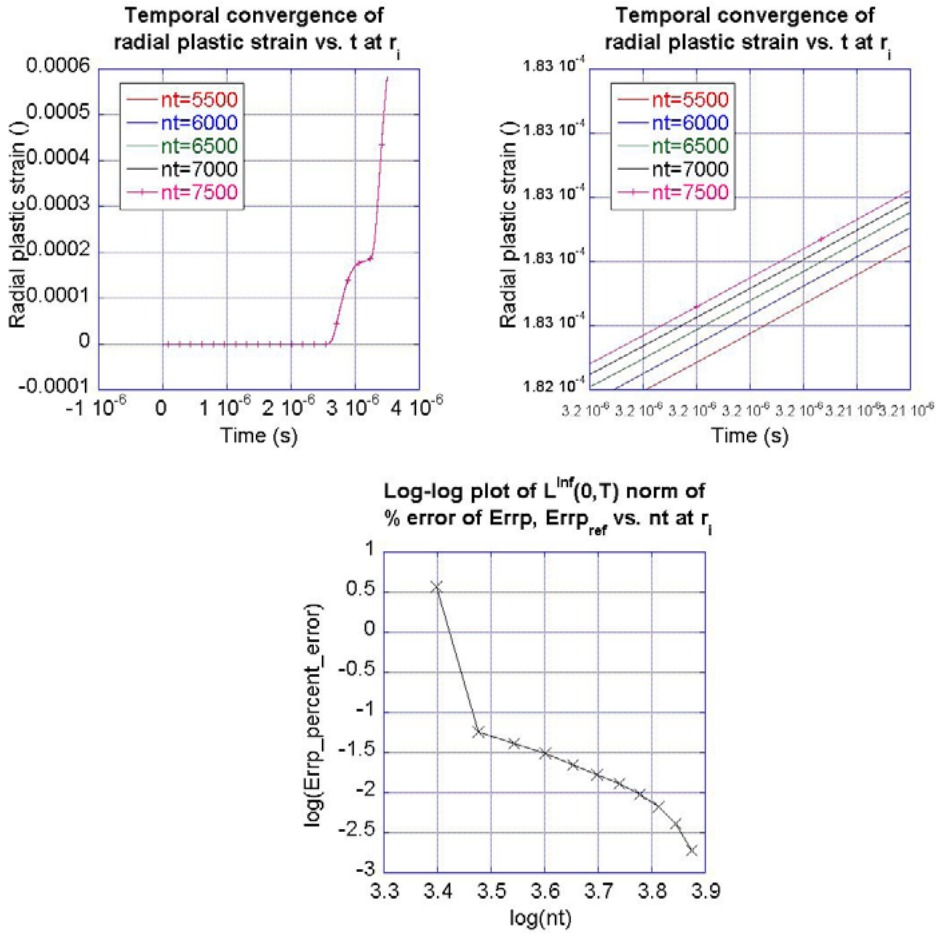

Figure 4: Top Left: Spatial convergence plot of ε^p_{rr} vs. t at inner radius. Top Right: Zoomed-in plot of ε^p_{rr}. Bottom: Log-log plot of $L^\infty(0,T)$ percent error of ε^p_{rr} at r_i vs. nt.

error approximately $10^{-1.27}\%$ when $nl = 300$. Therefore, since these errors are so small, we take $nl = 300$ as an appropriate eigenmode resolution for a "converged" solution. We argue that a "self-converged" benchmark analytic solution requires at least $nr = 3500$ uniform spatial intervals, $nt = 6500$ uniform time steps, and $nl = 300$ eigenmodes in the series solution.

5 Conclusions

In this paper we examine the dynamic sphere problem for a visco-plastic isotropic material following the Bodner-Partom (BP) model. The governing equations come from the balance of linear momentum in continuum mechanics formulated in material coordinates and the BP equations of plastic flow. We derive an analytic solution that has the form of an infinite series of Bessel functions. We establish convergence of our truncated solution

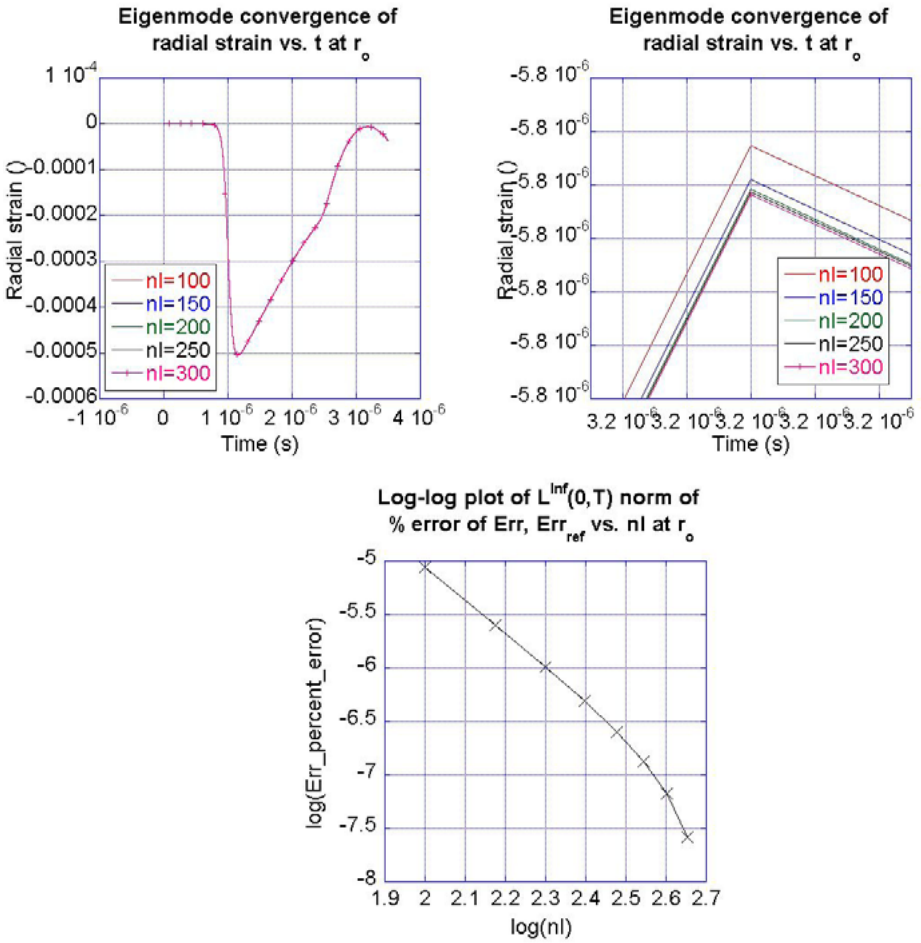

Figure 5: Top Left: Spatial convergence plot of ε_{rr} vs. t at outer radius. Top Right: Zoomed-in plot of ε_{rr}. Bottom: Log-log plot of $L^{\infty}(0,T)$ percent error of ε_{rr} at r_o vs. nl.

under different types of refinement for a particular test problem. We find for all fields of interest (displacement, velocity, strains, and stresses) that, under spatial refinement, the truncated solution exhibits errors of less than 0.001% under appropriate L^{∞} norms. Under temporal refinement, all fields of interest exhibit errors of less than 0.1% under appropriate L^{∞} norms. Finally, under eigenmode refinement, we see that all fields of interest exhibit errors of less than 0.01% under appropriate L^{∞} norms.

REFERENCES

[1] J. A. Sharpe, The Production of Elastic Waves by Explosion Pressures. I. Theory and Empirical Field Observations. *Geophysics* (1942) **7**:144–154.

[2] F. G. Blake. Spherical Wave Propagation in Solid Media. *Journal of Acoustical Society of America* (1952) **24**:211–215.

[3] G. J. Hutchens. An Exact Solution Code for the Blake Problem. Los Alamos National Laboratory. LA-UR-06-1097. (2006).

[4] L. E. Malvern. *Introduction to the Mechanics of a Continuous Medium*. Prentice-Hall Inc., (1969).

[5] T. O. Williams. Exact Solutions for the Spherically Symmetric Dynamic Response of Spherical Shells. Los Alamos National Laboratory. LA-UR-05-2660. (2005).

[6] T. O. Williams, S. Li, J. S. Brock, J. R. Kamm. Spherical Shell Analysis for Material Modeling. Los Alamos National Laboratory. LA-UR-05-8038. (2005).

[7] J. R. Kamm, T. O. Williams, J. S. Brock, S. Li. Application of Gegenbauer Polynomial Expansions to Mitigate Gibbs Phenomenon in Fourier-Bessel Series Solutions of a Dynamic Sphere Problem. *Commun. Numer. Meth. Engng.* (2010) **26, No. 10**:1276–1292.

[8] Bodner, S.R. and Partom, Y. Constitutive Equations for Elastic-Viscoplastic Strain-Hardening Materials. *J. of Appl. Mech.* (1975) 385–389.

[9] B. M. Chabaud, J. S. Brock, T. O. Williams. Transverse Isotropic Elastic Dynamic Sphere Problem. *6th European Congress on Computational Methods in Applied Sciences and Engineering, ECCOMAS 2012*. Vienna. (2012) 5736–5748.

[10] B. M. Chabaud, J. S. Brock, T. O. Williams, B. M. Smith. Benchmark Analytic Solution of the Dynamic Response of a Spherical Shell Composed of a Transverse Isotropic Elastic Material. *Int. J. Solids Struct.* (2013) Submitted.

[11] B. Chabaud, B. Smith, J. Brock. The Dynamic Sphere Test Problem. Los Alamos National Laboratory. LA-UR-12-21452. (2012).

[12] R. M. Jones. *Mechanics of Composite Materials*. Taylor & Francis, Second Edition, (1999).